

Control Strategies for Solution-Processed ZTO-Based Thin-Film Transistors Tailored Toward Volatile Organic Compound Detection

Lauren R. Miller,* Alejandro Galán-González,* Ben Nicholson, Leon Bowen, Guillaume Monier, Robert J. Borthwick, Freddie White, Mana Saeed, Richard L. Thompson, Christine Robert-Goumet, Del Atkinson, Dagou A. Zeze,* and Mujeeb U. Chaudhry

A breakthrough in the fabrication of amorphous Zn-Sn-O (ZTO)-based thin-film transistors (TFTs) is presented for volatile organic compound (VOC) detection. The incorporation of highly abundant materials offers substantial economic and environmental benefits. However, analyses for the design of a multilayer channel are still limited. This work demonstrates that the chemical environment influences ZTO-based TFTs' carrier transport properties and can be tailored for detecting specific VOCs, ensuring high specificity in diagnosing life-threatening conditions through simple breath analysis. A low-cost, high-throughput, fully solution-processed ZTO and ZnO multilayering strategy is adopted. The in-depth compositional and morphological analyses reveal that low surface roughness, excellent Zn and Sn intermixing, high oxygen vacancy (31.2%), and M-OH bonding (11.4%) contents may account for the outstanding electrical and sensing performance of ZTO-ZTO TFTs. Notably, these TFTs achieve near-zero threshold voltage (2.20 V), excellent switching properties (10^7), and high mobility ($10 \text{ cm}^2 \text{ V}^{-1} \text{ s}^{-1}$). This results in high responsivity to alcohol vapors at low-voltage operation with peak responsivity for methanol ($R = 1.08 \times 10^6$) over two orders of magnitude greater than acetone. When miniaturized, these devices serve as easy-to-operate sensors, capable of detecting VOCs with high specificity in ambient conditions.

1. Introduction

Abnormal concentrations of VOCs in human breath serve as disease-specific biomarkers for real-time, non-invasive diagnosis of medical conditions. One such example is methanol poisoning outbreaks after the consumption of adulterated alcohol, which frequently overwhelm healthcare facilities in developing countries with devastating consequences including organ failure, blindness, and even death.^[1–3] Rapid detection for the screening of laced beverages is vital and can be enabled by measuring methanol concentration in human breath. This concentration is ≈ 0.4 ppm for a healthy individual. However, laboratory-based screening tools such as gas chromatography-mass spectrometry typically require long processing times, trained professionals, and expensive instrumentation.^[4,5] Therefore, the development of point-of-care sensors that are simple to operate

L. R. Miller, F. White, M. Saeed, D. A. Zeze, M. U. Chaudhry
Department of Engineering
Durham University
Durham DH1 3LE, UK
E-mail: lauren.r.miller@durham.ac.uk; d.a.zeze@durham.ac.uk

A. Galán-González
Instituto de Carboquímica (ICB-CSIC)
C/ Miguel Luesma Castán 4, Zaragoza 50018, Spain
E-mail: agalan@icb.csic.es

B. Nicholson, L. Bowen, R. J. Borthwick, D. Atkinson
Department of Physics
Durham University
Durham DH1 3LE, UK

G. Monier, C. Robert-Goumet
Université Clermont Auvergne, Clermont Auvergne INP, CNRS, Institut Pascal
Clermont-Ferrand F-63000, France

R. L. Thompson
Department of Chemistry
Durham University
Durham DH1 3LE, UK

 The ORCID identification number(s) for the author(s) of this article can be found under <https://doi.org/10.1002/aelm.202400810>

© 2025 The Author(s). Advanced Electronic Materials published by Wiley-VCH GmbH. This is an open access article under the terms of the [Creative Commons Attribution](https://creativecommons.org/licenses/by/4.0/) License, which permits use, distribution and reproduction in any medium, provided the original work is properly cited.

DOI: 10.1002/aelm.202400810

and can distinguish methanol from other VOCs in ambient conditions has important societal benefits.^[6]

Chemiresistive gas sensors that incorporate highly abundant materials such as zinc oxide (ZnO), tin oxide (SnO₂), and ZTO have been widely publicized thanks to their high mobility, environmental stability, and ease of fabrication.^[7–15] Their working principle is straightforward and reversible, based on changes in the electrical resistance of the metal oxide when exposed to different concentrations of the target gases. Solution-processed TFTs have shown great promise for next-generation high throughput chemiresistive gas sensing for inexpensive point-of-care testing applications. The gate electrode modulates the conductivity of the TFT, and changes in drain-source current (I_{ds}) are measured between source-drain electrodes to yield an amplified response.^[16–18] Recently, we have demonstrated the facile detection of acetone vapors for the early symptom detection of diabetes using SnO₂ TFTs under ambient conditions. I_{ds} increased following exposure as acetone underwent a redox reaction with the adsorbed oxygen species on the semiconductor surface, which resulted in free electrons being released back into the conduction band.^[19]

Sensor responsivity (R) at low-voltage operation is dictated by two key parameters, current on/off ratio ($I_{on/off} \geq 10^7$) and threshold voltage (V_{th}), which should be near-zero to realize mobile applications with low power requirements. Zan et al. showed that low V_{th} (<5 V) and high $I_{on/off}$ (>10⁶) exhibited by amorphous In-Ga-Zn-O (a-IGZO) TFTs capped with an organic sensing layer led to high sensitivity to acetone vapor with a limit of detection of 100 ppb (see Table S9, Supporting Information).^[20] Various approaches have been reported to improve the chemiresistive properties of metal oxide TFTs, including defect engineering and Sn doping, by which their electronic structure and surface morphology can be precisely tuned. The introduction of oxygen vacancies promotes the chemisorption of oxygen molecules onto the metal oxide surface, enabling enhanced sensitivity and shortened response time for VOC detection.^[21] The latter involves the introduction of Sn, which can create smooth amorphous films and offers advantages with regard to large-scale uniformity and the possibility of miniaturization.^[22,23] The origin of the electrical and chemiresistive properties of single-layer TFTs is well understood.^[18] However, detailed morphological and structural analyses of stacked and alternating layers are limited to date. The design of a multilayer channel has been shown to enhance reliability and charge transport.^[24–26]

In this work, we demonstrate a strategy for enhanced functional performance via the multilayering of solution-processed metal oxide semiconductors. We used ZnCl₂ and SnCl₂ precursors to successfully fabricate bottom gate top contact TFTs grown by the sequential deposition and thermal treatment of ZTO and ZnO. The electrical properties of the ZTO-based TFTs were heavily influenced by several factors, including film composition, layering, and surface morphology. The judicious control of film thickness was facilitated by rigorous structural and compositional analyses of the multilayer metal oxide films. Secondly, we qualitatively assessed the interrelation between oxygen vacancy content and gas sensing performance to demonstrate VOC detection proof-of-concept. The resulting low power consumption and high signal-to-noise ratio of the measured functionality exceeds the existing literature and will facilitate a de-

tailed quantitative sensing study that will be reported in the future.^[27–31]

2. Results and Discussion

2.1. Optimization of the Charge Transport Layer

We adopted a simple design strategy to tailor the electrical and sensing performance of metal oxide TFTs, which involved the layering of spin-coated ZTO and ZnO thin films. ZnO was studied as it is well-known that ZnO nanostructures grown on the surface of ZTO enhance electron injection in other solution-processed devices.^[32] To highlight the benefit of controlling film thickness and morphology via the sequential spin-casting and thermal treatment of metal oxide layers, our preliminary study compared the electronic performance of a single-layer ZTO TFT prepared from a precursor solution with double the concentration against the ZTO-ZTO TFT presented in Figure 1a. Next, we assessed the thermal treatment of ZTO-ZTO bilayer films by annealing the layers at increasing temperatures. Figure 1a shows a schematic of the device and Figure 1b, the TGA. A detailed description is given in supporting information (Figure S1 and Table S2, Supporting Information). We then compared the electrical performance of monolayer and bilayer ZTO-based TFTs treated at the optimum temperature of 500 °C. The spin-coating parameters were maintained at 5000 rpm for 30 s to control the film thickness and ensure long-range homogeneity. Effective mobility (μ_{eff}) and V_{th} of the ZTO-ZTO TFTs were extracted using Equations (1)–(4) from the I_{ds} against applied gate bias, V_{gs} , transfer characteristics presented in Figure 1c.

Electronically, the ZTO TFT performed poorly in comparison to the ZTO-ZTO TFT, owing to pronounced hysteresis in the I_{ds} – V_{gs} measurements, which leads to a large V_{th} shift from –7.44 to 3.84 V for the forward and backward sweeps of V_{gs} , respectively. Conversely, the ZTO-ZTO TFT exhibited excellent stability and minimal V_{th} shift, calculated as 2.20 and 2.31 V for the forward and backward sweeps, respectively. Based on this successful result, a multilayering approach, involving the intercalation of a ZnO layer to construct bilayer and trilayer TFTs was explored. The resulting multilayers were all thermally treated at 500 °C following the previously discussed results, and their transfer characteristics are presented in Figure 1d.^[33] The ZTO-ZnO TFT exhibited large hysteresis, poor carrier mobility ($\mu_{eff} = 0.135 \text{ cm}^2\text{V}^{-1}\text{s}^{-1}$) and $I_{on/off} < 10^4$ than the former ZTO-ZTO TFT. In addition, the electrical properties of the ZTO-ZTO-ZnO TFT were inferior to those calculated for the ZTO-ZnO-ZTO TFT, which suggests that the deposition of the final ZnO layer impeded the efficiency of charge transport between the source-drain electrodes. Importantly, the low off-current and near-zero V_{th} of the ZTO-ZTO and ZTO-ZnO-ZTO TFTs allude that a high responsivity could be achieved at low-voltage operation in the presence of VOCs. The electronic parameters are summarized in Table 1.

2.2. Growth and Structural Characterization Metal Oxide Layers

To understand the physical basis of the enhanced electronic functionality, a detailed structural investigation was undertaken. The

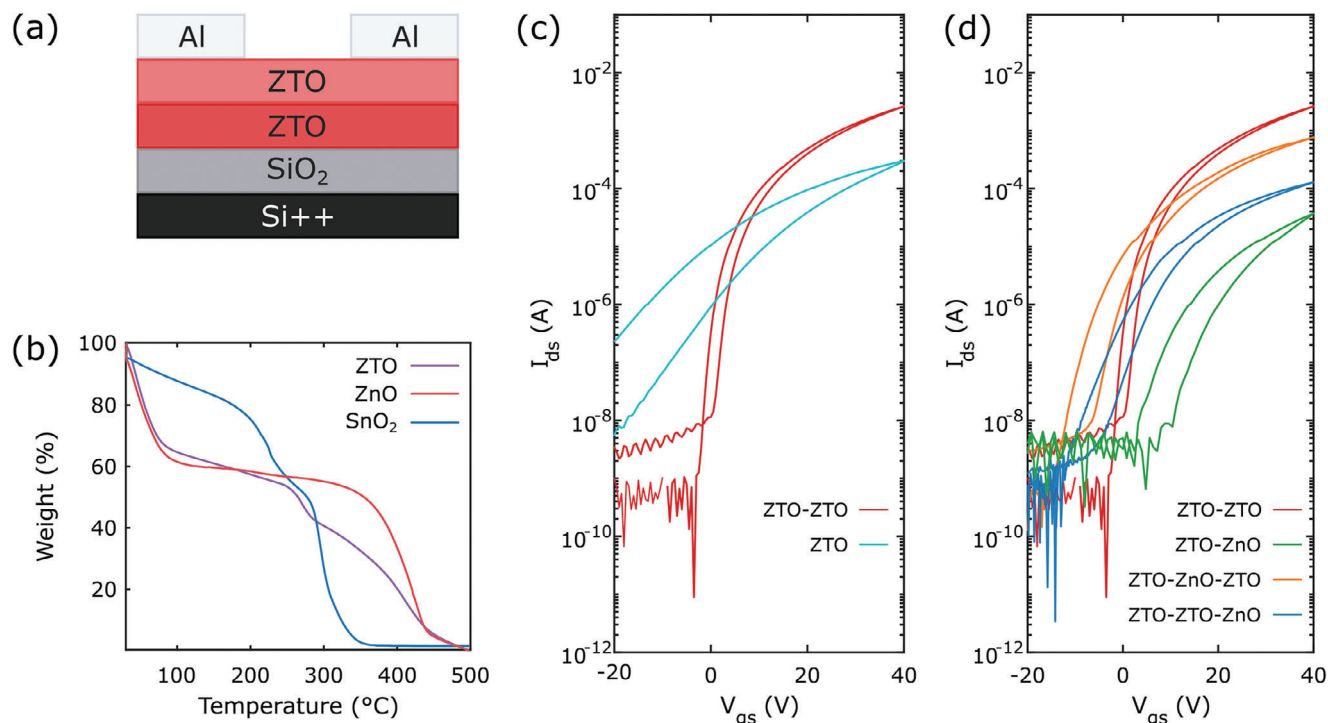


Figure 1. a) Schematic of ZTO-ZTO TFT. b) TGA curves for ZTO, ZnO, and SnO₂ solutions. c) Transfer characteristics in the saturation regime at $V_{ds} = 40$ V and $V_{gs} = -20$ to 40 V for the ZTO and ZTO-ZTO TFTs treated at 500 °C. d) Transfer characteristics in the saturation regime at $V_{ds} = 40$ V and $V_{gs} = -20$ to 40 V for the bilayer and trilayer TFTs treated at 500 °C.

effect of inserting a ZnO layer on the crystalline properties of the ZTO-based films was investigated using X-ray reflectometry (XRR) and X-ray diffraction (XRD). The XRR results examined the interface width, film thickness, and density of the metal oxide systems.^[26] **Figure 2a** shows that the period of these Kiessig fringes and fall in intensity were related to differences in film thickness and total interface width of the layers, respectively.^[26,34] The lower number of oscillating fringes for the monolayer compared to the bilayer and trilayer systems, are well represented by the best-fitting simulations (solid black lines, Table S3, Supporting Information), indicating that the monolayer is a thinner film. The position of the critical angle also shifted toward higher

Table 1. Electrical parameters obtained from monolayer and multilayer metal oxide TFTs treated at 500 °C.

Device	$I_{on/off}$	V_{th} [V]	μ [$\text{cm}^2\text{V}^{-1}\text{s}^{-1}$]	μ_{eff} [$\text{cm}^2\text{V}^{-1}\text{s}^{-1}$]
ZTO	10^6	-7.44	0.775	0.741
ZTO	10^4	5.36	0.148	0.135
ZnO				
ZTO	10^7	2.20	10.2	9.49
ZTO				
ZTO	10^6	-1.74	2.55	2.32
ZnO				
ZTO				
ZTO	10^5	-0.910	0.458	0.417
ZnO				

angles, which points toward denser films after the second and third layers were spin-coated and thermally treated. The curve shape around the critical angle was broader for the multilayer stacks, which suggests that the film density was not constant throughout the bulk of the bilayer and trilayer films.

The best-fitting simulations of the XRR results were used to determine the scattering length density (SLD) plotted in **Figure 2b**, which shows that the effective density increased from ≈ 0.8 to 1.3 g cm^{-3} for the monolayer and bilayer films at the substrate ($Z \approx 0$ nm), respectively. Film density remained constant before reaching the ZTO and ZTO-ZnO film surfaces, however, a clear drop was observed in the bulk of the ZTO-ZTO film at $Z \approx 7$ nm. The same behavior was observed for the trilayer systems as the film depth approached 10 nm, in agreement with the broadening around the critical angle. We infer that our spin-coated films were not organized in a traditional layer-by-layer heterostructure system with a single uniform interface. Instead, the first layer was compacted by the addition and thermal treatment of the second and third layers, giving rise to two distinct regions with different film densities.

Specular XRR cannot distinguish between topographical roughness and chemical intermixing of the interference between layers. Therefore, the variation in total interface width with sample depth shown by the shaded areas of **Figure 2b** considered both of these interface-broadening mechanisms. The thickness of the ZTO film was estimated to be roughly 8 nm, which increased to over 15 nm for the ZTO-ZTO film. Furthermore, the surface of these two films may have been smooth as the Kiessig fringes were observed at higher angles ($2\theta > 3.5^\circ$). Conversely, the thickness of

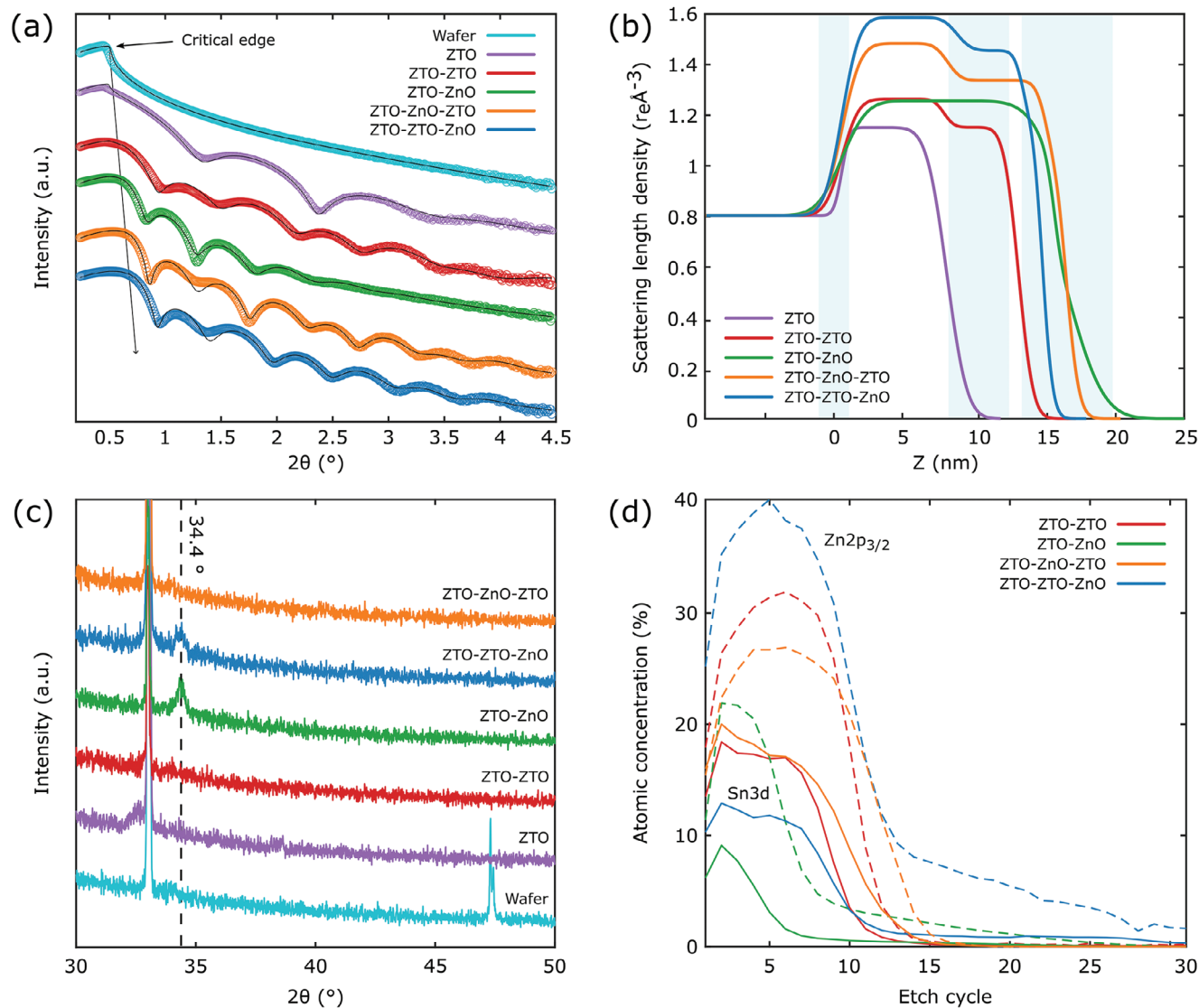


Figure 2. a) Measured (symbols) and calculated (solid black lines) XRR spectra obtained from single, bilayer, and trilayer metal oxide systems. b) Extracted SLD versus depth profile (Z) for $2\theta = 0$ to 4.5° . c) XRD measurements for $2\theta = 30$ to 50° . d) XPS depth profile of Zn $2p_{3/2}$ and Sn $3d$.

the ZTO-ZnO film was notably more than that of the ZTO-ZTO film (>20 nm), which, coupled with the Kiessig fringes only being present at lower angles ($2\theta < 2.5^\circ$), suggested a much rougher surface morphology than the other films. The maximum densities of the trilayer films were consistent with the movement of the critical angle toward $2\theta \approx 1^\circ$ and were between 1.4 and $1.6 \text{ r}_e \text{ \AA}^{-3}$, correlating with the addition of the third layer and compaction of the initial deposition.

XRD indicated that the ZTO-capped films (ZTO-ZTO and ZTO-ZnO-ZTO) were amorphous as they did not exhibit sharp diffraction peaks assignable to a crystalline phase (Figure 2c). These results are comparable with those of solution-processed films prepared using metal chlorides dissolved in 2-methoxyethanol at similar conditions reported in the literature.^[30,35–38] Nonetheless, the ZnO-capped films (ZTO-ZnO and ZTO-ZTO-ZnO) showed a small halo at $2\theta \approx 34.4^\circ$, ascribed to the hexagonal wurtzite structure of ZnO (002).^[39] The origin

of this peak could be explained by the growth of Zn single-crystal nanoparticles, which caused the increase in surface roughness and film thickness.

Finally, X-ray photoelectron spectroscopy (XPS) depth profiling was conducted to track the evolution of the Zn $2p_{3/2}$ and Sn $3d$ peak intensities and assess the possible gradients or migration of either component in our TFTs. Etch cycle zero corresponded to the film surface, and the etching was considered complete when the main signals present were the Si $2s$, Si $2p$, and O $1s$ peaks of the substrate, from etch cycle ten to twenty depending on the thickness of the film (Figures S5, and S6, Supporting Information). Figure 2d shows clear differences in Zn and Sn composition following the introduction of a ZnO layer. The ZTO-capped samples comprised films homogeneous in thickness and Zn/Sn distribution on the surface of the substrate, as the Zn $2p_{3/2}$ and Sn $3d$ signals diminished following the eighth etch cycle. It was noted that the Zn $2p_{3/2}$ and Sn $3d$ signals reached a

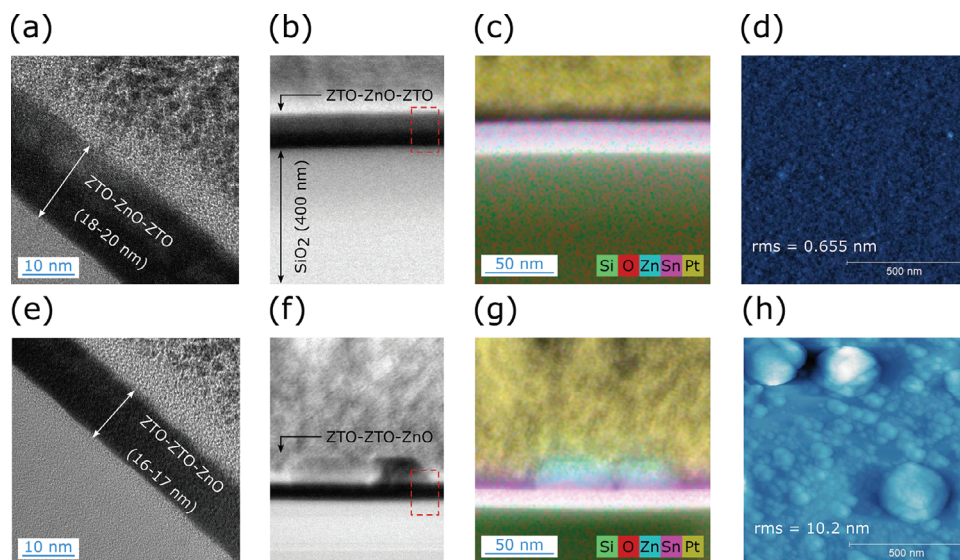


Figure 3. Morphological analysis of the a–d) ZTO-ZnO-ZTO and e–h) ZTO-ZTO-ZnO films. a,e) High- and b,f) low-magnification TEM images (red dashed square). c,g) Elemental mapping. d,h) AFM images ($1 \mu\text{m}^2$ scan area) with calculated rms surface roughness.

plateau at maximum intensity around etch cycle five, which concurred with the two distinct regions of film density observed from XRR analysis. Conversely, the Zn $2p_{3/2}$ signal was still prominent beyond etch cycle twenty-five for the ZnO-capped samples. Furthermore, the signature of the Sn 3d signal rose sharply before reaching maximum intensity and was markedly reduced with respect to the Zn $2p_{3/2}$ signal for the ZTO-ZnO sample. The latter correlates well with the XRD results, which suggested Zn crystal growth in addition to the target material. The ZTO-ZnO film density also remained constant throughout the bulk of the film, indicative of a single-layer film that was predominantly Zn. Finally, the low metallic content recorded for the ZTO-ZnO film may have explained the poor electronic performance of the ZTO-ZnO TFT.

To further investigate the clear differences in surface morphology and composition between the ZnO- and ZTO-capped films, TEM, SEM, and AFM analyses were carried out on ZTO-ZnO-ZTO (Figure 3a–d) and ZTO-ZTO-ZnO films (Figure 3e–h), respectively.

The high-magnification TEM image (Figure 3a) of the ZTO-ZnO-ZTO sample shows a homogenous film that has a thickness between 18 and 20 nm over a large region of the TFT (Figure 3b), in good agreement with XRR analysis. Complementary elemental mapping (Figure 3c; Figure S2a–e, Supporting Information) supports the evolution of the Zn $2p_{3/2}$ and Sn 3d signals as the components were well mixed throughout the entire film. The AFM and SEM images (Figure 3d; Figures S3a,b, and S4a,c,d, Supporting Information) of the ZTO-capped samples show amorphous films with surface roughness comparable to that of the substrate (0.655 nm),^[32] consistent with XRD analysis, while, the TEM images (Figure 3e,f) of the ZTO-ZTO-ZnO film confirmed the growth of crystalline features up to a micron in height, composed primarily of Zn observed from the elemental mapping of Figure 3g and Figure S2f–j (Supporting Information). As mentioned, these Zn single crystals brought about the small halo observed during XRD analysis at $2\theta \approx 34.4^\circ$ that corresponded to

the hexagonal wurtzite structure of ZnO (002).^[32] The AFM and SEM images (Figure 3h; Figures S3c, and S4b, Supporting Information) of the ZnO-capped samples display increased surface roughness (10.2 nm) as a result of the small particles grown on the surface. These were accompanied by micron-sized crystalline features observed in the high-magnification TEM and were dispersed randomly on the surface of the substrate with a large distribution of particle sizes. The final ZTO layer may have helped to planarize the film surface, which facilitated the cleaner deposition of source-drain electrodes and the establishment of charge percolation pathways that may be responsible for the enhanced electrical performance of the ZTO-capped TFTs.

Considering now the electronic environment, Figure 4a,b shows the XPS spectra for the Zn $2p_{3/2}$ and Sn 3d components, which were calibrated against the C 1s peak centered at 284.6 eV to adjust for any charge-induced shift during testing. The shift of Zn $2p_{3/2}$ peak to lower binding energy points toward increased oxygen vacancy content.^[40] The binding energies at 486.5 and 495 eV are separated by 8.5 eV and ascribed to Sn $3d_{5/2}$ and Sn $3d_{3/2}$ core levels, indicating the Sn⁴⁺ oxidation state.^[22] Therefore, Sn²⁺ of SnCl₂ in the precursor turned into Sn⁴⁺ in our ZTO films after thermal treatment at 500 °C in the air, which is the main component for n-type conduction.^[41,42] The presence of Sn has been known to enhance carrier density and suppress electron scattering effects due to the ionic radii of Zn²⁺ (0.074 nm) and Sn⁴⁺ (0.069 nm).^[22,23] The ZTO-capped films comprised the highest Sn content, calculated as 16.9% and 17.2%, respectively, for the bilayer and trilayer TFTs (Table S5, Supporting Information). In contrast, the ZTO-ZnO film contained the lowest Sn content (3.1%), attributed to the introduction of the ZnO final layer, which resulted in the formation of the aforementioned rough, particulate film. It is inferred that the low Sn content was responsible for the exceptionally low mobility calculated for the ZTO-ZnO TFT.

The presence of oxygen vacancies is commonly regarded as a major factor in the generation and separation of charge

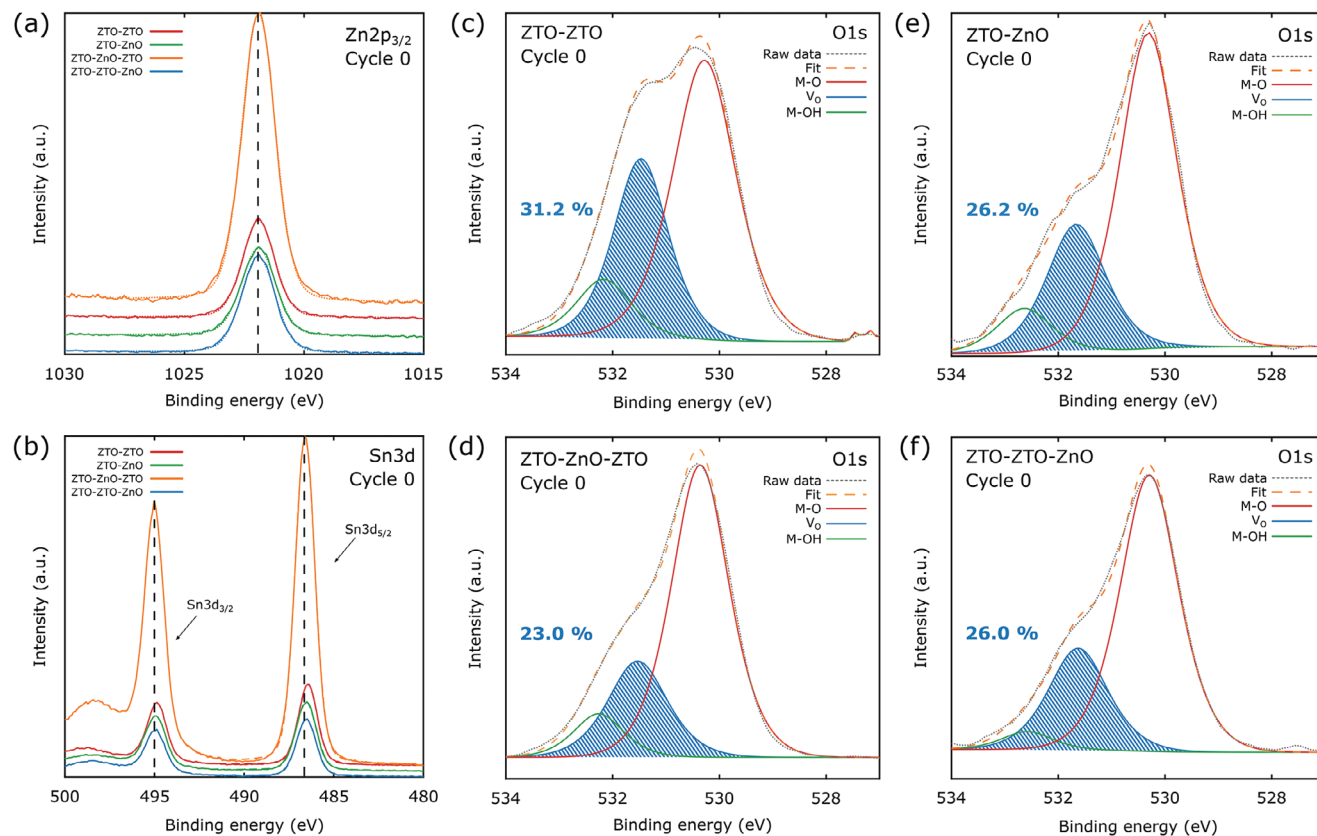


Figure 4. XPS core level spectra of a) Zn $2p_{3/2}$ and b) Sn 3d. XPS core level spectra of c–f) O 1s for ZTO-ZTO, ZTO-ZnO-ZTO, ZTO-ZnO, and ZTO-ZTO-ZnO films, respectively.

carriers within ZnO-based films. Interestingly, high oxygen vacancy content in metal oxides can also promote the adsorption of relevant gases and accommodate more chemisorbed oxygen species that enhance sensitivity and shorten the response time for VOC detection.^[21] Therefore, we conducted an in-depth analysis of the O 1s peak in our metal oxide systems to couple oxygen vacancy content with the electronic properties, so that the most appropriate films could be taken forward as chemiresistive gas sensors. The O 1s peak was deconvoluted into three components through Gaussian–Lorentzian fitting, shown in Figure 4c–f. The lower binding energy component at 530.3 eV was associated with the oxygen bonded to metal atoms (M–O),^[41] while the higher binding energy component at 531.5 eV corresponded to an oxygen-deficient region, related to oxygen vacancy content (V_O) in the metal oxide thin films.^[28] Finally, the component centered at 533.4 eV was ascribed to the presence of loosely bound oxygen, such as hydroxide (M–OH).^[43] The ZTO-ZnO-ZTO film contained the largest proportion of M–O = 70.1% (Table S4, Supporting Information), responsible for the high density observed from XRR analysis, while the ZTO-ZTO film contained the lowest percentage of M–O = 57.8%. However, Figure 4c shows that the shape of the O 1s envelope for this film was significantly different from the other systems, with a large shoulder created by the large content fraction associated with oxygen vacancies. The ZTO-ZTO film contained the largest proportion of V_O = 31.2%. In addition, Table S4 (Supporting Information) further lists that the ZTO-ZTO film comprised the largest proportion of M–OH

= 11.4%, which could act as additional adsorption sites. On the other hand, the ZTO-ZnO-ZTO film comprised little M–OH = 3.9%.

The improved electrical performance of the metal oxide TFTs can be primarily attributed to more charge carrier generation by Sn. We also consider that the rougher active layer surface and larger particle size due to the growth of Zn single crystals heavily impact the charge transport between source-drain electrodes, hence, the ZTO-capped TFTs exhibit superior switching properties compared to the ZnO-capped TFTs. They also show near-zero V_{th} , making them ideal candidates for VOC detection within a low-voltage window. Therefore, the ZTO-ZTO TFT was taken forward and tested for VOC detection. The TFT was exposed to methanol to provide a benchmark sensor response since it possessed the highest oxygen vacancy content. The ZTO-ZTO film also contained the highest M–OH states, which was expected to encourage high responsivity toward methanol specifically, due to the presence of the hydroxyl groups. To qualitatively assess the specificity of the ZTO-ZTO TFT to methanol, its chemiresistive responses following overnight exposure to other VOCs, specifically acetone, IPA, and toluene, were tested.

2.3. Detection of VOCs in the Air Using ZTO-ZTO TFTs

The ZTO-ZTO TFT treated at 500 °C was exposed to methanol vapor overnight to quantify its performance as a chemiresistive

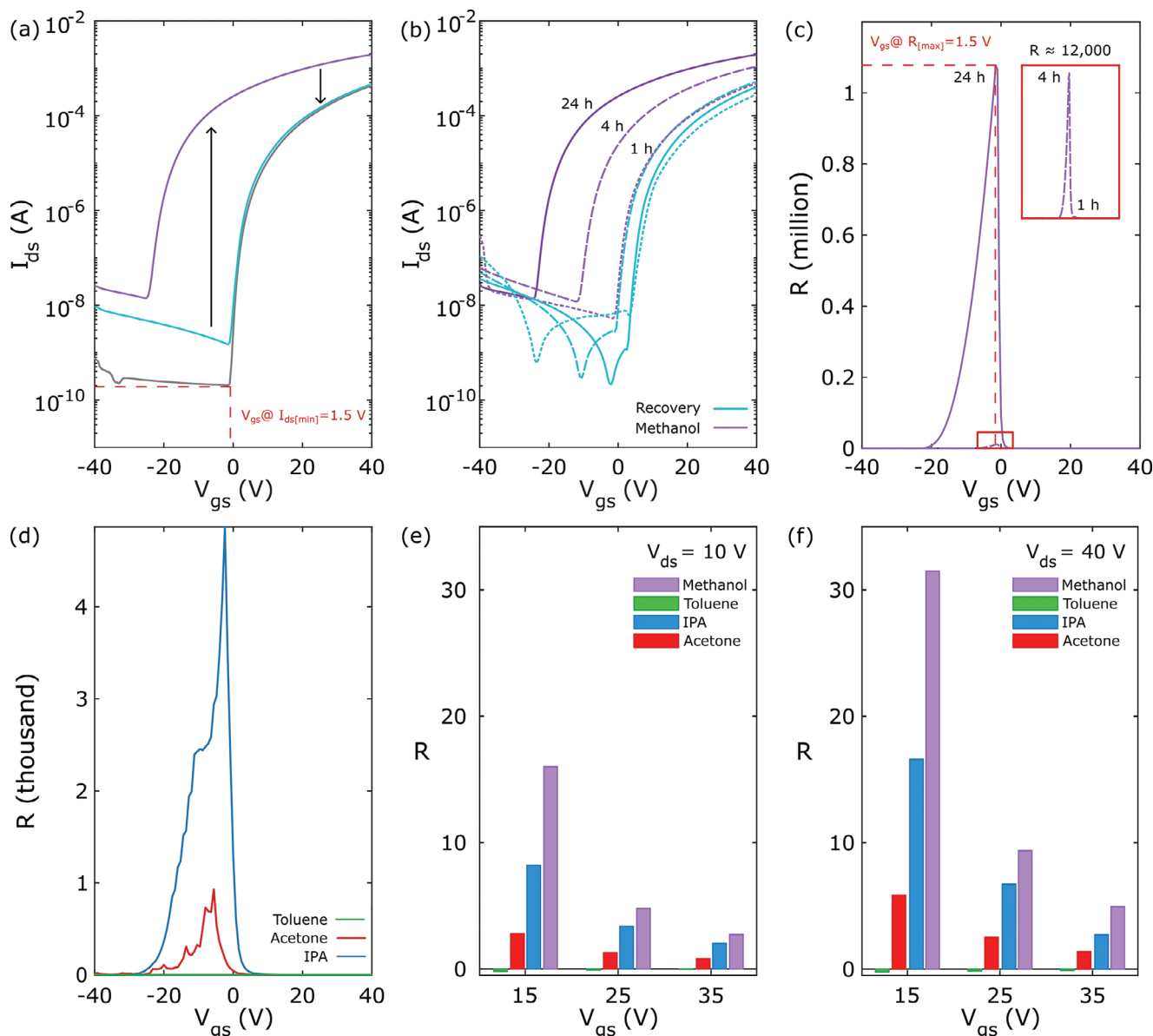


Figure 5. a) Transfer characteristics in the saturation regime at $V_{ds} = 40$ V, $V_{gs} = -40$ to 40 V, and $L = 80$ μm following overnight exposure to methanol vapor and recovery with heat treatment. b) Dynamic sensor response and c) calculated responsivity following 1 h, 4 h (inset, dashed purple lines) and 24 h exposure periods. d) Calculated responsivity following overnight exposure to toluene, acetone, and IPA vapors. e) Transient sensor response at fixed $V_{gs} = 15$, 25, and 35 V in the linear and f) saturation regimes.

gas sensor. These experiments were conducted in a maintained cleanroom environment under controlled conditions (Class 1000, RH = 45.5%, $T = 19.2$ $^{\circ}\text{C}$) in the air, i.e., not inside a N_2 glovebox. **Figure 5a** shows that V_{th} and $I_{ds[\text{max}]}$ increased after exposure, which suggested a decrease in the electrical resistance of the film during adsorption and desorption of gas molecules on the surface. The chemiresistive response (R) of the ZTO-ZTO TFT was calculated by measuring the relative change in I_{ds} (Equation 5). Changes in the position at which maximum responsivity was achieved relied upon the V_{gs} at the minimum drain-source current, $I_{ds[\text{min}]}$, prior to V_{th} (see Figure 5a,c). The magnitude of the maximum responsivity attained was also governed by the

$I_{on/off}$ of the as-prepared TFTs, respectively. In this case, $I_{ds[\text{min}]}$ of the as-prepared ZTO-ZTO TFT was measured at $V_{gs} = -1.50$ V and maximum responsivity ($R = 1.08 \times 10^6$) was also achieved at this point. The electronic parameters for the as-prepared TFTs as well as after exposure and recovery with heat treatment are summarized in **Table 2**. As it can be observed, the recovery of the device is almost complete after desorption of methanol for 15 min since all of the metrics return to values close to those prior to exposure. This indicates that our TFT sensors were very reliable, which is paramount for this type of application.

To further assess our ZTO-ZTO sensor's reliability and reproducibility, its dynamic response, shown in Figure 5b, was

Table 2. Electrical properties for $L = 80 \mu\text{m}$ obtained before and after the ZTO-ZTO TFTs treated at 500°C were exposed to methanol in the air overnight.

	$I_{\text{on/off}}$	V_{th} [V]	μ [$\text{cm}^2\text{V}^{-1}\text{s}^{-1}$]	μ_{eff} [$\text{cm}^2\text{V}^{-1}\text{s}^{-1}$]
Before exposure	10^7	3.14	5.21	4.66
Methanol	10^5	-23.3	8.90	8.62
Recovery	10^6	2.63	5.48	4.95

measured following short (1 h), long (4 h), and overnight (24 h) exposure periods. The ZTO-ZTO TFT was recovered with heat treatment for 15 min as previously described after each exposure cycle (cyan lines).

To confirm our specificity to vapors that contain the -OH hydroxyl group, we exposed the ZTO-ZTO TFT to acetone, IPA, and toluene. Toluene, a subclass of VOCs with aromatic rings, can serve as an important biomarker for cancer. Indeed, abnormally high concentrations of toluene have been observed in the exhaled breath of patients with lung cancer compared to healthy non-smokers.^[44] The good specificity of a sensor for aromatic compounds like toluene depends chiefly on the previously mentioned chemical environment of the sensing material, the decomposition rate of the adsorbed molecule on the surface, and operation temperature. The calculated responsivity following overnight exposure shown in Figure 5c (24 h, solid purple lines) far surpassed that measured for acetone, IPA, and toluene vapors. In fact, our ZTO-ZTO TFT was more responsive ($R = 11\,400$) after exposure to methanol for 4 h (Figure 5c) inset, dashed purple lines) compared with overnight exposure to acetone ($R = 9330$). Our ZTO-ZTO TFT sensors were highly specific to vapors that contain the -OH hydroxyl group because of their high oxygen vacancy and M-OH bonding contents, which acted as specific adsorption sites. It is inferred that the methanol vapor adsorbed on the ZTO-ZTO surface more easily than IPA owing to its much lower vapor pressure, size, and molecular weight. In contrast, the responsivity signature obtained following exposure to acetone was much less, possibly due to the reduced polarity of the -C=O carbonyl group. Now, Figure 5d shows that the relative change in I_{ds} after overnight exposure to toluene at room temperature was negligible, which alluded that the toluene vapor, specifically the methyl group, was less prone to adsorption and desorption on the ZTO-ZTO surface compared to the other reducing vapors.

Finally, Figure 5e,f shows the transient responses of the ZTO-ZTO TFT at fixed $V_{\text{gs}} = 15, 25, \text{ and } 35 \text{ V}$ in the linear and saturation regimes, $V_{\text{ds}} = 10 \text{ and } 40 \text{ V}$, respectively. In both regimes, responsivity is maximized as V_{gs} approaches the V_{th} of the as-prepared TFTs following exposure to oxygen-related VOCs: acetone, IPA, and methanol. The ZTO-ZTO TFT was clearly more sensitive to these vapors in the saturation regime, governed by Equation (1).

Methanol underwent a redox reaction with adsorbed oxygen on the ZTO-ZTO surface (Equations 6–7, supporting information).^[18,40] Due to the large electronegativity of oxygen atoms, adsorbed oxygen depleted electrons from the metal oxide film during thermal treatment, which increased its resistance and formed reduced oxygen species at room temperature.^[45,46] The high density of oxygen vacancies in the ZTO-ZTO film acted

as acceptors of oxygen ion species in ambient conditions, creating a thicker depletion layer. Increased charge density in the vicinity of the valence band maximum and conduction band minimum due to these oxygen vacancies, possibly narrow the bandgap, which may have favored the adsorption of target gas molecules.^[21,47] Specific sites for the adsorption of hydroxyl groups also mean that methanol molecules interact with a greater number of oxygen ion species leading to a significant increase in I_{ds} , which is consistent with free electrons being released back into the conduction band. These changes resulted primarily from the reduction reaction with adsorbed oxygen on the ZTO-ZTO film surface and were unaffected by the presence of grain boundaries because of the amorphous nature of the layer.^[7] The difference in sensing characteristics suggested that ZTO-ZTO TFTs could achieve accurate cross-sensitivity toward exhaled breath containing multiple gases and high responsivity at the V_{gs} required for a battery-driven chemiresistive gas sensor.

3. Conclusion

To conclude, the electrical performance of ZTO-based TFTs has been tailored by adopting a ZTO and ZnO multilayering design strategy for improved chemiresistive response. The addition of a ZnO layer significantly influenced the crystalline and morphological properties of the metal oxide films. The ZTO-capped TFTs yielded better electrical performance, while a ZnO capping layer caused the growth of ZnO particles, which created a much rougher film surface with worsened source-drain contacts. With this in mind, the ZTO-ZTO TFT achieved near-zero threshold voltage ($V_{\text{th}} = 2.20 \text{ V}$) and excellent switching properties ($I_{\text{on/off}} = 10^7$) while maintaining high mobility ($\mu_{\text{eff}} \approx 10 \text{ cm}^2\text{V}^{-1}\text{s}^{-1}$). Its low surface roughness, superb Zn and Sn intermixing, high oxygen vacancy (31.2%) and M-OH bonding (11.4%) contents show that this TFT was deemed an ideal chemiresistive sensor and subsequently exposed to a variety of VOCs with different functional groups, specifically acetone, IPA, methanol, and toluene. Our qualitative analyses demonstrated a high responsivity to alcohol vapors at low-voltage operation with peak responsivity for methanol ($R = 1.08 \times 10^6$) over two orders of magnitude greater than acetone. We have shown that the chemical environment influences the carrier transport properties of ZTO-based TFTs and can be tailored toward the detection of specific VOCs, ensuring that high specificity can be achieved for the diagnosis of life-threatening conditions by simple breath analysis.

4. Experimental Section

Transistor Fabrication: The substrates consisted of a 400 nm SiO_2 dielectric on a highly doped Si wafer, which acted as the back gate. They were cleaned by sonication in acetone and IPA ($\geq 99.5\%$ from Sigma-Aldrich) separately for 15 min to remove debris, fibers, or inorganic contaminants and blow-dried with N_2 . Finally, they were placed in a UV ozone cleaner (Novascan) for 1 h to remove oils, fingerprints, or organic contaminants. This process also increased the wettability of the substrates prior to spin-coating and ensured that a uniform layer of material was deposited with the desired thickness. The precursor solutions were prepared under a fume hood. ZnCl_2 and SnCl_2 (150 mm, anhydrous, 99.999% from Sigma-Aldrich) powders were dissolved in 2-methoxyethanol separately and sonicated for 15 min. The ZTO solution was prepared by mixing equal amounts

of ZnCl₂ and SnCl₂ (1:1) precursor solutions and was aged under stirring for 24 h at room temperature. The ZTO and ZnO solutions were filtered through a syringe filter (0.42 μm) and spin-coated onto the cleaned substrates under a fume hood. The multilayer films were grown by the sequential deposition and thermal treatment of ZTO and ZnO at temperatures in the range of 300–500 °C. After deposition and thermal treatment, 50 nm thick Al source-drain electrodes were deposited via thermal evaporation using a shadow mask under a high vacuum (≈10⁻⁶ mbar) in an evaporation chamber integrated within an N₂ glovebox.

Characterization and Measurements: The electrical characterization of the TFTs was performed in ambient conditions using two Agilent B2912A semiconductor parameter analyzers. The bespoke chamber (Figure S11, Supporting Information) was manufactured to record changes in transfer characteristics upon exposure to reducing vapors.

The thermal behavior of the ZTO, ZnO, and SnO₂ solutions was examined using thermal gravimetric analysis (TGA) (Perkin Elmer Pyris 1 TGA) at a heating rate of 10 °C min⁻¹ from 30 to 500 °C in the air. Data processing was completed using the complementary software package, Pyris.

The crystalline properties of the films were determined using XRD and XRR (Bruker AXS D8 Advance GX003410). Surface morphology was examined by AFM (Asylum Research MFP-3D Infinity). Image processing and analysis were performed using the open-source software Gwyddion.

The chemical states of the metal oxide films were examined using XPS surface and depth profiling analyses. XPS measurements were carried out in a SPECS ProvenXPS system equipped with a PHOIBOS 150 2D-CMOS hemispherical analyzer and a monochromatic X-ray source FOCUS 500. The Al Kα X-ray source (1486.6 eV) operated at 400 W and was separated from the analyzer by 55°. A medium magnification mode and constant pass energy of the analyzer equal to 20 eV were used for analysis. Photoelectron data were recorded at a take-off angle of 90° (normal detection). The survey spectrum and the high-resolution spectra were recorded with an energy step of 0.5 eV over 1400 and 0.1 eV, respectively. Binding energies, line widths, and areas of the different XPS peaks were obtained by a weighted least-squares fitting of a Gaussian-Lorentzian model curve to the experimental data using the program CasaXPS. For depth profiling analyses, the samples were etched using an Ar ion gun at 2 keV with a sample current density of 0.5 μAcm⁻². The etch cycle duration was 60 s, and the rate was approximated as 0.025 ± 0.05 nm s⁻¹. The atomic concentrations were calculated assuming that the analyzed depth was homogeneous.

Field emission SEM (FESEM) images of the ZTO-ZTO-ZnO and ZTO-ZnO-ZTO films were obtained by using a FEI Helios Nanolab 600 at 15 kV. High-resolution TEM (HRTEM) and energy-dispersive X-ray spectroscopy (EDX) were carried out in a JEOL 2100F FEG at 200 kV, equipped with an Oxford Instruments Aztec microanalysis system. The cross-sectional samples were prepared in the FESEM system, equipped with a Ga-focused ion beam (FIB) source. The Pt was deposited on the films prior to FIB milling to ensure a smooth and clean cross-section was obtained.

Calculation of Effective Mobility: Assuming that μ is independent of V_{gs} and neglecting short channel effects, I_{ds} in the saturation regime are given by Equation (1):^[48]

$$I_{ds} = \frac{WC_i}{2L} \mu (V_{gs} - V_{th})^2 \quad (1)$$

where I_{ds} is the drain current, $\frac{W}{L}$ is the channel width-to-length ratio, C_i is the capacitance per unit area of the dielectric layer, μ is the charge carrier mobility, V_{gs} is the gate voltage and V_{th} is the threshold voltage. μ is obtained by taking the partial derivative with respect to V_{gs}. Rearranging the resulting equation yields Equation (2):

$$\mu = \frac{2L}{WC_i} \left(\frac{\partial \sqrt{I_{ds}}}{\partial V_{gs}} \right)^2 \quad (2)$$

$\frac{\partial \sqrt{I_{ds}}}{\partial V_{gs}}$ can be extracted by plotting $\sqrt{I_{ds}}$ against V_{gs} and finding the gradient. Ideal transfer characteristics are linear and hence $\frac{\partial \sqrt{I_{ds}}}{\partial V_{gs}}$ is constant.

In practice, external factors such as contact resistance can produce curved plots, which has resulted in several erroneous reported mobilities. The reliability factor (r) given in Equation (3) accounts for nonlinearities in transfer characteristics.^[48] It is defined as the ratio (expressed in %) of the maximum channel conductivity experimentally achieved in a FET to that calculated in an equivalent ideal FET:

$$r = \frac{\left(\frac{\sqrt{|I_{ds}|^{max}} - \sqrt{|I_{ds}|^0}}{|V_{gs}|^{max}} \right)^2}{\left(\frac{WC_i}{2L} \mu \right)_{claimed}^2} \quad (3)$$

where $\left(\frac{WC_i}{2L} \mu \right)_{claimed}^2$ accounts for the claimed device parameters and mobility in the saturation regime. |I_{ds}|^{max} is the experimental maximum drain current reached at the maximum gate voltage, |V_{gs}|^{max}. |I_{ds}|⁰ is the drain current at V_{gs} = 0. Effective mobility, μ_{eff}, is thus given by:

$$\mu_{eff} = \mu \times r \quad (4)$$

The values quoted in this report are μ_{eff} and calculated using C_i = 9 nFcm⁻² and W = 3 mm. L = 80 μm unless otherwise stated.

Calculation of Responsivity: The chemiresistive responses of the TFT gas sensors were measured using the sealed custom-built testing rig shown in Figure S11 (Supporting Information). An open 3 mL vial was filled with solvent and placed in the chamber, which was allowed to evaporate overnight to ensure that the sensor was saturated with the target vapor. The TFT was retested before the taps on the chamber were opened in a fume cupboard. Afterwards, it was removed and heated at 100 °C for 15 min to recover I_{ds}. In general, the sensitivity of conventional chemiresistive gas sensors has been expressed as a ratio of resistance or drain current variation. R was calculated using:^[18,19,49]

$$R = \frac{\Delta I_{ds}}{I_{ds}[0]} = \frac{I_{ds}[gas] - I_{ds}[0]}{I_{ds}[0]} \quad (5)$$

where ΔI_{ds} represents the difference in I_{ds} before (I_{ds}[0]) and following (I_{ds}[gas]) exposure to reducing vapors.

Supporting Information

Supporting Information is available from the Wiley Online Library or from the author.

Acknowledgements

M.U.C. thanks the Engineering and Physical Sciences Research Council (EPSRC) (New Investigator Award # EP/V037862/1 and Capital Equipment Grant EC/RF080422) for financial support. A.G.G. acknowledges funding from Spanish MCIN (MCIN/AEI/10.13039/501100011033) and “ERDF A way of making Europe” under project grant PID2022-139671OB-I00, as well from the Gobierno de Aragón (DGA) under projects T03_23R (Grupos de Investigación Reconocidos). G.M. gratefully acknowledges financial support from the project SASS AV0027152 from FEDER-FSE-2014-2020 and the project 16-IDEX-0001 CAP 20–25. L.M. thanks DAMG and LB for early experimentation and constructive discussion during the XPS analysis.

Conflict of Interest

The authors declare no conflict of interest.

Data Availability Statement

The datasets presented during this study are available from the authors on reasonable request.

Keywords

amorphous, metal oxide, solution-processed, thin-film transistor, volatile organic compounds

Received: October 24, 2024

Revised: December 18, 2024

Published online:

- [1] Z. Nekoukar, Z. Zakariaei, F. Taghizadeh, F. Musavi, E. S. Banimostafavi, A. Sharifpour, N. E. Ghuchi, M. Fakhari, R. Tabaripour, S. Safanavaei, *Ann. Med. Surg.* **2021**, *66*, 102445.
- [2] A. Mashallahi, M. Mohamadkhani, A. Ostadtaghizadeh, *Iran J. Public Health* **2021**, *50*, 1502.
- [3] J. van den Broek, S. Abegg, S. E. Pratsinis, A. T. Güntner, *Nat. Commun.* **2019**, *10*, 4220.
- [4] M. Phillips, K. Gleeson, J. M. B. Hughes, J. Greenberg, R. N. Cataneo, L. Baker, W. P. McVay, *Lancet* **1999**, *353*, 1930.
- [5] G. Peng, U. Tisch, O. Adams, M. Hakim, N. Shehada, Y. Y. Broza, S. Billan, R. Abdah-Bortnyak, A. Kuten, H. Haick, *Nat. Nanotech.* **2009**, *4*, 669.
- [6] H. C. Ates, C. Dincer, *Nat. Rev. Bioeng* **2023**, *1*, 80.
- [7] K. S. Kim, C. H. Ahn, S. H. Jung, S. W. Cho, H. K. Cho, *ACS Appl. Mater. Interfaces* **2018**, *10*, 10185.
- [8] Y. Shimizu, A. Jono, T. Hyodo, M. Egashira, *Sens. Actuators, B.* **2005**, *108*, 56.
- [9] N. Barsan, U. Weimar, *J. Electroceram.* **2001**, *7*, 143.
- [10] G. Korotcenkov, *Mater. Sci. Eng., B.* **2007**, *139*, 1.
- [11] S. J. Patil, A. V. Patil, C. G. Dighavkar, K. S. Thakare, R. Y. Borase, S. J. Nandre, N. G. Deshpande, R. R. Ahire, *Front. Mater. Sci.* **2015**, *9*, 14.
- [12] L. Jiang, J. Li, K. Huang, S. Li, Q. Wang, Z. Sun, T. Mei, J. Wang, L. Zhang, N. Wang, X. Wang, *ACS Omega* **2017**, *2*, 8990.
- [13] B. N. Pal, B. M. Dhar, K. C. See, H. E. Katz, *Nat. Mater.* **2009**, *8*, 898.
- [14] T. Kamiya, K. Nomura, H. Hosono, *Sci. Technol. Adv. Mater.* **2010**, *11*, 044305.
- [15] T. Kamiya, K. Nomura, H. Hosono, *J. Disp. Technol.* **2009**, *5*, 273.
- [16] A.-M. Andringa, J. R. Meijboom, E. C. P. Smits, S. G. J. Mathijssen, P. W. M. Blom, D. M. de Leeuw, *Adv. Funct. Mater.* **2011**, *21*, 100.
- [17] K.-W. Kao, M.-C. Hsu, Y.-H. Chang, S. Gwo, J. A. Yeh, *Sensors* **2012**, *12*, 7157.
- [18] J. Li, L. Li, Q. Chen, W. Zhu, J. Zhang, *J. Mater. Chem. C.* **2022**, *10*, 860.
- [19] L. R. Miller, R. J. Borthwick, P. L. dos Santos, M. U. Chaudhry, *MRS Advances* **2023**, *8*, 440.
- [20] H.-W. Zan, C.-H. Li, C.-C. Yeh, M.-Z. Dai, H.-F. Meng, C.-C. Tsai, *Appl. Phys. Lett.* **2011**, *98*, 253503.
- [21] H. Yuan, S. A. A. Aljineibi, J. Yuan, Y. Wang, H. Liu, J. Fang, C. Tang, X. Yan, H. Cai, Y. Gu, S. J. Pennycook, J. Tao, D. Zhao, *Adv. Mater.* **2019**, *31*, 1807161.
- [22] S. Ruzgar, M. Caglar, *J. Mater. Sci.: Mater. Electron.* **2019**, *30*, 485.
- [23] L.-C. Liu, J.-S. Chen, J.-S. Jeng, W.-Y. Chen, *ECS J. Solid State Sci. Technol.* **2013**, *2*, Q59.
- [24] K. Hu, Z. Guo, J. Wang, C. Lu, M. Wang, T. Wang, F. Liao, G. Yang, N. Lu, L. Li, *Adv. Electron. Mater.* **2024**, 2400266.
- [25] W. Cai, M. Li, S. Lu, Q. Qian, Z. Zang, *IEEE Trans. Electron Devices* **2023**, *70*, 3085.
- [26] Y. Lin, H. Faber, J. G. Labram, E. Stratakis, L. Sygellou, E. Kymakis, N. A. Hastas, R. Li, K. Zhao, A. Amassian, N. D. Treat, M. McLachlan, T. D. Anthopoulos, *Adv. Sci.* **2015**, *2*, 1500058.
- [27] K. Muhieddine, M. Ullah, B. N. Pal, P. Burn, E. B. Namdas, *Adv. Mater.* **2014**, *26*, 6410.
- [28] Q. Zhang, G. Xia, L. Li, W. Xia, H. Gong, S. Wang, *Curr. Appl. Phys.* **2019**, *19*, 174.
- [29] S. Sanctis, N. Koslowski, R. Hoffmann, C. Guhl, E. Erdem, S. Weber, J. J. Schneider, *ACS Appl. Mater. Interfaces* **2017**, *9*, 21328.
- [30] S.-J. Seo, C. G. Choi, Y. H. Hwang, B.-S. Bae, *J. Phys. D: Appl. Phys.* **2008**, *42*, 035106.
- [31] A. Liu, Z. Guo, G. Liu, C. Zhu, H. Zhu, B. Shin, E. Fortunato, R. Martins, F. Shan, *Adv. Electron. Mater.* **2017**, *3*, 1600513.
- [32] A. Galán-González, P. Pander, R. C. I. MacKenzie, L. Bowen, D. A. Zeze, R. J. Borthwick, R. L. Thompson, F. B. Dias, M. U. Chaudhry, *ACS Photonics* **2023**, *10*, 4315.
- [33] R. D. Chandra, M. Rao, K. Zhang, R. R. Prabhakar, C. Shi, J. Zhang, S. G. Mhaisalkar, N. Mathews, *ACS Appl. Mater. Interfaces* **2014**, *6*, 773.
- [34] C. Swindells, H. Głowiński, Y. Choi, D. Haskel, P. P. Michałowski, T. Hase, P. Kuświk, D. Atkinson, *Appl. Phys. Lett.* **2021**, *119*, 152401.
- [35] P. K. Nayak, M. N. Hedhili, D. Cha, H. N. Alshareef, *ACS Appl. Mater. Interfaces* **2013**, *5*, 3587.
- [36] Y. J. Kim, B. S. Yang, S. Oh, S. J. Han, H. W. Lee, J. Heo, J. K. Jeong, H. J. Kim, *ACS Appl. Mater. Interfaces* **2013**, *5*, 3255.
- [37] M.-G. Kim, H. S. Kim, Y.-G. Ha, J. He, M. G. Kanatzidis, A. Facchetti, T. J. Marks, *J. Am. Chem. Soc.* **2010**, *132*, 10352.
- [38] D. Ho, H. Jeong, H.-B. Park, S. K. Park, M.-G. Kim, C. Kim, *J. Mater. Chem. C.* **2023**, *11*, 13395.
- [39] Y. Zhou, S.-T. Han, L. Zhou, Y. Yan, L.-B. Huang, J. Huang, V. A. L. Roy, *J. Mater. Chem. C.* **2013**, *1*, 7073.
- [40] J. Lee, Y. Choi, B. J. Park, J. W. Han, H.-S. Lee, J. H. Park, W. Lee, *J. Adv. Ceram.* **2022**, *11*, 769.
- [41] M. Lei, L. Guo, C. Wang, C. Wang, X. Chu, F. Yang, X. Gao, H. Wang, Y. Chi, X. Yang, *J. Mater. Sci.: Mater. Electron.* **2022**, *33*, 24785.
- [42] G. Gordillo, L. C. Moreno, W. de la Cruz, P. Teheran, *Thin Solid Films* **1994**, *252*, 61.
- [43] Y. R. Denny, K. Lee, S. Seo, S. K. Oh, H. J. Kang, D. S. Yang, S. Heo, J. G. Chung, J. C. Lee, *Appl. Surf. Sci.* **2014**, *315*, 454.
- [44] A. Mirzaei, J.-H. Kim, H. W. Kim, S. S. Kim, *J. Mater. Chem. C* **2018**, *6*, 4342.
- [45] H. Windischmann, P. Mark, *J. Electrochem. Soc.* **1979**, *126*, 627.
- [46] Y. Chen, H. Qin, Y. Cao, H. Zhang, J. Hu, *Sensors* **2018**, *18*, 3425.
- [47] J. Wang, Z. Wang, B. Huang, Y. Ma, Y. Liu, X. Qin, X. Zhang, Y. Dai, *ACS Appl. Mater. Interfaces* **2012**, *4*, 4024.
- [48] H. H. Choi, K. Cho, C. D. Frisbie, H. Sirringhaus, V. Podzorov, *Nat. Mater.* **2018**, *17*, 2.
- [49] M. T. Vijjapu, S. G. Surya, S. Yuvaraja, X. Zhang, H. N. Alshareef, K. N. Salama, *ACS Sens.* **2020**, *5*, 984.